



## Modelling the kinetics of NO oxidation and $\text{NO}_x$ storage over platinum, ceria and ceria zirconia

Kirsten Leistner<sup>a,b,\*</sup>, André Nicolle<sup>b</sup>, Patrick Da Costa<sup>a</sup>

<sup>a</sup> Université Pierre et Marie Curie - UPMC Paris 6, Institut Jean Le Rond D'Alembert, CNRS UMR 7190, 2 place de la gare de ceinture, 78210 Saint Cyr l'Ecole, France

<sup>b</sup> IFP Energies nouvelles, 1-4 avenue de Bois-Préau, 92852 Rueil-Malmaison, France

### ARTICLE INFO

#### Article history:

Received 12 July 2011

Received in revised form 19 October 2011

Accepted 21 October 2011

Available online 29 October 2011

#### Keywords:

Ceria

Zirconia

Platinum

$\text{NO}_x$

Kinetics

### ABSTRACT

The kinetics of  $\text{NO}_x$  oxidation and storage were studied over  $\text{Pt}/\text{Al}_2\text{O}_3$ ,  $\text{Ce}_x\text{Zr}_{1-x}\text{O}_2$  and  $\text{Pt}/\text{CeO}_2$ . A detailed kinetic mechanism involving lumped nitrate and nitrite species was proposed for the interaction of  $\text{NO}_x$  and  $\text{O}_2$  with ceria(-zirconia) and its parameters estimated using oxidation and adsorption/desorption experiments. Important trends in the behaviour of ceria-zirconia catalysts ( $x=0\text{--}0.84$ ), platinum and  $\text{Pt}/\text{CeO}_2$  were reproduced over a wide range of temperatures. Thus zirconium affects redox behaviour of the oxide, ultimately decreasing its ability to oxidise NO to  $\text{NO}_2$ .  $\text{NO}_x$  storage is described via the accumulation of nitrates on the oxide surface. Oxidation and storage over  $\text{Pt}/\text{CeO}_2$  can be reproduced by fitting ceria and platinum-related parameters separately. While oxidation behaviour is mainly dictated by Pt, nitrate storage occurs on  $\text{CeO}_2$  and is shown to be more efficient under a  $\text{NO}+\text{O}_2$  flow than  $\text{NO}_2$ . However when considering an equal number of active sites,  $\text{Pt}/\text{CeO}_2$  stores  $\text{NO}_x$  less efficiently than  $\text{Pt}/\text{BaO}/\text{Al}_2\text{O}_3$ .

© 2011 Elsevier B.V. All rights reserved.

### 1. Introduction

In the context of evermore stringent requirements in terms of fuel efficiency and  $\text{CO}_2$  emissions, lean-burn engines are becoming a solution preferable to stoichiometric gasoline engines [1]. However, the development of exhaust gas treatment technologies, such as lean  $\text{NO}_x$  traps (LNTs), for emission abatement from lean-burn engines still represents a challenge. The oxidation of NO to  $\text{NO}_2$  is crucial in a number of exhaust gas treatment processes. These include  $\text{NO}_x$  removal with LNTs [1] and the oxidation of soot in catalysed diesel particulate filters (DPFs) [2,3]. The  $\text{NO}_x$  storage-reduction (NSR) catalysts used in LNTs typically contain noble metals for  $\text{NO}_x$  oxidation and reduction and alkali/alkali earth metal compounds for  $\text{NO}_x$  storage [1]. The use of  $\text{CeO}_2$  and  $\text{CeO}_2\text{--ZrO}_2$  mixed oxides as either storage component or support is common in DPFs [3–6], LNTs [7,5,6] and in three-way catalysts because of the oxides' oxygen storage capacity [8–10]. These applications mostly see ceria(-zirconia) as a part of composite catalyst formulations and few articles investigate the NSR behaviour of these oxides on their own. The  $\text{NO}_x$  trapping performance of the storage component is generally assumed to occur in the form of sorbed nitrites or nitrates on its basic adsorption sites [1]. The common NSR

catalyst  $\text{Pt}/\text{BaO}/\text{Al}_2\text{O}_3$  is known to adsorb  $\text{NO}_2$  more efficiently than NO [11,12] and in this case the oxidation of NO to  $\text{NO}_2$  prior to the storage phase is a definite advantage. While with  $\text{Pt}/\text{BaO}/\text{Al}_2\text{O}_3$ , NO oxidation takes place mainly over Pt,  $\text{CeO}_2$  has been shown to be an "active" support, capable of acting as an oxidation catalyst itself [13]. Dispersed Pt particles on ceria-zirconia are known to resist ageing better than the common  $\text{Pt}/\text{BaO}/\text{Al}_2\text{O}_3$  [14]. Most studies employ complex gas flows; few investigate the role and especially the kinetics of  $\text{NO}_x$  oxidation/storage in simpler systems such as  $\text{Pt}/\text{CeO}_2$  and  $\text{Pt}/\text{CeO}_2\text{--ZrO}_2$  under  $\text{O}_2/\text{NO}/\text{NO}_2$  streams [15,13]. Although many data obtained by first principles calculations [16–18] help understand the reaction mechanism, most of these cannot be directly employed in mean-field kinetic models because they are sensitive to the structure of the crystal lattice and site heterogeneity in general, and these aspects are not taken into account in our kinetic approach. Overall, the role of ceria in NSR remains controversial [1]. While some studies [19,20] demonstrate that  $\text{NO}_x$  storage benefits from the addition of ceria to Ba-based NSR catalysts, others [21] observe no noticeable effect. In order to fully understand the complex mechanism of exhaust gas catalysis, it is appropriate to study all the involved phenomena separately. Therefore the present paper deals with  $\text{NO}/\text{O}_2$  and  $\text{NO}_2$  gas feeds only. Parameters pertaining to these different experimental gas feeds are determined separately. These values are determined by fitting model equations to data of temperature-programmed experiments, a technique which is well known [22,23]. Based on data from literature, this study aims to elucidate the kinetics of NO

\* Corresponding author at: IFP Energies nouvelles, 1-4 avenue de Bois-Préau, 92852 Rueil-Malmaison, France.

E-mail address: [kirsten.leistner@ifpen.fr](mailto:kirsten.leistner@ifpen.fr) (K. Leistner).

oxidation in a simple gas flow over  $\text{CeO}_2$  and  $\text{CeO}_2\text{--ZrO}_2$ , and model the main  $\text{NO}_x$ -oxidation–storage trends over a  $\text{Pt}/\text{CeO}_2\text{--ZrO}_2$  NSR catalyst.

## 2. Modelling approach

### 2.1. Reactor model

The reactor experiments simulated during the course of this study involve a reactive gaseous flow over a fixed bed of catalyst particles. Experiments with monoliths are also modelled as equivalent fixed beds. The reactor model describing the reactive flow in the fixed bed system was coded in C++ and equations are solved using the IFP-Exhaust library of the AMESim (LMS.IMAGINE.Lab) environment. The modelling approach of this software is based on bond-graph theory, according to which any physical system can be represented by resistive and capacitive elements in an electrical analogy [24]. For all studied cases, preliminary calculation of the Peclet number confirms that the fixed bed may be modelled by a single continuously stirred reactor. In the AMESim environment, each 0D reactor is composed of capacitive and resistive elements. Capacitive elements are similar to an open volume where pressure and temperature are deduced from mass and energy balances, whereas resistive elements are used to compute mass and enthalpy flow rates using Darcy's law for flow in porous media, as explained previously [12]. The mass balance equation for a gaseous species  $i$  in a capacitive element is hence:

$$\frac{dm_i}{dt} = \dot{m}_i^{in} - \dot{m}_i^{out} + \omega_i \quad [\text{kg/s}] \quad (1)$$

where  $\dot{m}_i$  are the mass flow rates in and out of the capacitive element and  $\omega_i$  is the chemical source term for species  $i$ . Section 2.2 explains how  $\omega_i$  is calculated. External diffusion limitations are typically not significant in fixed bed reactors at the low operating temperatures in use [25]. However, the elementary model addresses potential mass transfer limitations due to intra-particle (or internal) diffusion, following the Thiele approach already adopted earlier on [26]. For all cases simulated during the course of this study, the Thiele modulus remains much smaller than 0.3 and the reactor can therefore be considered to operate in the kinetic regime.

### 2.2. Surface chemistry model

A piece-wise approach was followed in the construction of the model. In order to obtain physically meaningful parameters, reaction subsets of the mechanism had to be tested and validated against a number of experiments with simple reactive gas flows, such as  $\text{O}_2$  or  $\text{NO} + \text{O}_2$  alone. The different “blocks” thus obtained were then assembled and validated with data from the composite system. In particular, R1–R2 in Table 1 were calibrated alone using data from reaction of cerium oxides with  $\text{O}_2$ . Similarly, R3–R8 were calibrated using experiments performed with cerium oxides under an atmosphere of  $\text{NO} + \text{O}_2$ , while leaving the parameters of R1–R2 unchanged. In the same way,  $\text{Pt} + \text{O}_2$  and  $\text{Pt} + \text{O}_2 + \text{NO}$  experiments were used to determine the parameters of R9–R10 and R11–R16, respectively. Both TPD and oxidation experiments were used for calibration. The model is therefore able to reproduce catalyst adsorption and desorption behaviour as well as the NO oxidation by  $\text{O}_2$ . Thus, although the number of fitted parameters is large, the model is also required to be compatible with a number of species concentrations ( $\text{O}_2$ , NO and  $\text{NO}_2$ ) and experimental conditions (TPD, TPD, Pt only,  $\text{CeO}_2$  only, differing composition of reactive flow). Furthermore, all simulated experiments are temperature-programmed, which means that extrapolated kinetics are valid for a large range of temperatures [22] (100–700 °C). Minor species such

**Table 1**

Surface reaction mechanism of the interaction of  $\text{NO}_x$  and  $\text{O}_2$  with ceria and platinum.

#### Reactions on support

- R1:  $2\text{Ce}^{3+} + \text{O}_2 \rightarrow 2\text{Ce}^{4+}\text{--O}$
- R2:  $2\text{Ce}^{4+}\text{--O} \rightarrow 2\text{Ce}^{3+} + \text{O}_2$
- R3:  $\text{Ce}^{3+} + \text{NO}_2 \rightarrow \text{Ce--NO}_2$
- R4:  $\text{Ce--NO}_2 \rightarrow \text{Ce}^{3+} + \text{NO}_2$
- R5:  $\text{Ce--NO}_2 \rightarrow \text{Ce}^{4+}\text{--O} + \text{NO}$
- R6:  $\text{Ce}^{4+}\text{--O} + \text{NO} \rightarrow \text{Ce--NO}_2$
- R7:  $\text{Ce--NO}_2 + \text{Ce}^{4+}\text{--O} \rightarrow \text{Ce--NO}_3 + \text{Ce}^{3+}$
- R8:  $\text{Ce}^{3+} + \text{Ce--NO}_3 \rightarrow \text{Ce--NO}_2 + \text{Ce}^{4+}\text{--O}$

#### Reactions on platinum

- R9:  $2\text{Pt} + \text{O}_2 \rightarrow 2\text{Pt--O}$
- R10:  $2\text{Pt--O} \rightarrow 2\text{Pt} + \text{O}_2$
- R11:  $\text{Pt} + \text{NO} \rightarrow \text{Pt--NO}$
- R12:  $\text{Pt--NO} \rightarrow \text{Pt} + \text{NO}$
- R13:  $\text{Pt--NO} + \text{Pt--O} \rightarrow \text{Pt--NO}_2$
- R14:  $\text{Pt--NO}_2 \rightarrow \text{Pt--NO} + \text{Pt--O}$
- R15:  $\text{Pt} + \text{NO}_2 \rightarrow \text{Pt--NO}_2$
- R16:  $\text{Pt--NO}_2 \rightarrow \text{Pt} + \text{NO}_2$

as  $\text{N}_2$  and  $\text{N}_2\text{O}$  were not included in the mechanism. Apart from the two Ce–O surface species, the mechanism involves two kinds of Ce–N and Pt–N as well as one Pt–O surface species, all of which are lumped representations of intermediates which may be observed experimentally. No measurements of surface concentrations were available for fitting, but a survey of the literature gives temperature intervals of stability for these species, which can be used to ascertain whether surface behaviour of the model is reasonable. It was assumed that constants calibrated against  $\text{Pt}/\text{Al}_2\text{O}_3$  could be used to simulate either Pt alone or  $\text{Pt}/\text{Al}_2\text{O}_3$  within more complex catalytic systems, thus effectively neglecting the impact of the alumina support on the oxidative activity of the catalyst. The model is based on the mean field approximation, with the assumption that adsorbed species are randomly distributed on the surface, which is viewed as being locally uniform. Site heterogeneity is thus averaged out by mean rate coefficients [27,28]. The chemical source terms  $\omega_i$  for gaseous species  $i$  are calculated according to Eq. (2),

$$\omega_i = S_a M_i \sum_{j=1}^N v_{i,j} r_j \quad [\text{kg/s}] \quad (2)$$

where  $S_a$  and  $M_i$ , respectively are the active surface area of the catalyst considered and molar mass of the  $i$ -th gas-phase species,  $N$  is the total number of reactions considered,  $v_{i,j}$  the corresponding stoichiometric coefficients and  $r_j$  the reaction rate of the  $j$ -th reaction in  $\text{mol}/\text{m}^2/\text{s}$ . The molar rates of the forward and backward reactions listed in Table 1, are calculated according to the Arrhenius law (Eq. (3)),

$$r_j = A_j \exp \left( \frac{-E_j}{RT} \right) \left( \prod_{i=1}^{N_g} v_{i,j} x_i \prod_{k=1}^{N_s} v_{i,j} \theta_k \right) \quad [\text{mol}/\text{m}^2/\text{s}] \quad (3)$$

where  $A_j$  are the pre-exponential factors,  $E_j$  the activation energies in  $\text{kJ/mol}$ ,  $x_i$  the mole fraction of species  $i$  and  $\theta_k$  the dimensionless coverage of surface species  $k$  and  $N_g$  and  $N_s$  the number of gas and surface species, respectively.

Surface coverage of the  $k$ -th surface species,  $\theta_k$ , is described via:

$$\frac{d\theta_k}{dt} = \frac{r_k}{\Gamma} \quad (4)$$

in which  $r_k$  is the rate of generation or consumption of species  $k$  due to adsorption, desorption or chemical reaction and  $\Gamma$  the material-specific site density of the catalyst considered, in  $\text{mol}/\text{m}^2$ . For  $\text{CeO}_2$ , site density is taken to be  $2.7 \times 10^{-5} \text{ mol}/\text{m}^2$ , whereas for Pt, a value of  $1.7 \times 10^{-5} \text{ mol}/\text{m}^2$  is used [11].

**Table 2**  
Experiments used for model validation.

Catalyst	$x_{\text{NO}}$	$x_{\text{O}_2}$	Temperature	Figure	Type	Ref
$\text{Ce}_{1.0}\text{Zr}_{0.0}\text{O}_2$	0	$10^{-3}; 10^{-5}$	1200 °C; 1725 °C	n/a <sup>d</sup>	n/a	[32] <sup>a</sup>
$\text{Ce}_x\text{Zr}_{1-x}\text{O}_2$ <sup>b</sup>	0.0005	0.05	10 °C/min	1,3	TPO	[33]
$\text{Ce}_x\text{Zr}_{1-x}\text{O}_2$ <sup>c</sup>	0	0	10 °C/min	2,6	TPD <sup>e</sup>	[33]
7.7 wt% Pt/Al <sub>2</sub> O <sub>3</sub>	0	0	40 °C/min	7	TPD <sup>f</sup>	[34]
2.3 wt% Pt/Al <sub>2</sub> O <sub>3</sub>	0.0006	0.08	5 °C/min	8	TPO	[34]

<sup>a</sup> The model was compatible with the phase diagram in [32].

<sup>b</sup> Values of  $x$  were 1, 0.76, 0.56, 0.36 and 0.16.

<sup>c</sup> Values of  $x$  were 1 and 0.76.

<sup>d</sup> Not applicable.

<sup>e</sup> After adsorption of 200 ppm NO + 5% O<sub>2</sub> at 350 °C.

<sup>f</sup> After adsorption of 2% O<sub>2</sub> at 400 °C.

Reactions R1–R8 are elementary steps proposed to describe the global reaction  $2\text{NO} + \text{O}_2 \rightleftharpoons 2\text{NO}_2$ . Pre-exponential factors are given in the compatible units (using cm, mol and s), making it possible to readily implement the scheme in the Chemkin code [28] too. Adsorption rate constants are entered in the form of a dimensionless sticking coefficient  $S_{0,j}$ . The pre-exponential factor is then calculated as

$$A_{\text{ads}} = S_{0,j} \sqrt{\frac{RT}{2\pi M_i}} \quad (5)$$

The mechanism for CeO<sub>2</sub> (Reactions R1–R8) was proposed and optimised as explained in Section 3.1. A choice was made to employ the same surface mechanism to describe the behaviour of both CeO<sub>2</sub> and a range of CeO<sub>2</sub>–ZrO<sub>2</sub> mixed oxides (Ce<sub>x</sub>Zr<sub>1-x</sub>O<sub>2</sub>). Since the reducibility of Ce<sub>x</sub>Zr<sub>1-x</sub>O<sub>2</sub> is strongly dependent on the Zr content of the material [29,30], the kinetic parameters of R2 were adjusted to reproduce differing NO oxidation activity of Ce<sub>x</sub>Zr<sub>1-x</sub>O<sub>2</sub>. We proposed the mechanism involving Pt (Reactions R9–R16) in a previous study [11]. Kinetic parameters have however been optimised during the course of the present study. The current approach also differs from the previous study in that kinetic backward constants are fitted to experimental data at high temperature to ensure the reaction reaches equilibrium consistently with thermodynamics. Note that this study does not describe structural aspects of the catalytic system in detail, as catalysts are represented globally, via an active surface. Our focus here is on the derivation of kinetic parameters for the reaction steps in Table 1.

### 3. Results and discussion

Experiments simulated in Sections 3.1, 3.2 and 3.3 are listed in Table 2. The parameters obtained by calibration of the model or taken from literature are given in Table 3. Generally speaking, models in automotive catalysis are only reliable for the exact catalyst on which they have been tested [31]. Therefore our aim was to identify lumped reaction intermediates and reaction steps which are characteristic of the class of Ce<sub>x</sub>Zr<sub>1-x</sub>O<sub>2</sub> catalysts as a whole. These features should not be dependent on the precise conditions of synthesis and storage of the catalyst before the experiment. For instance, Ce–NO<sub>2</sub>, Ce–NO<sub>3</sub>, Ce<sup>3+</sup> and Ce<sup>4+</sup> were proposed because an extensive survey of the relevant literature showed that these species and their interactions have been identified in measurements from several different sources. We tried to minimise the possibility of non-unique sets of values by fitting the same parameters with several experimental profiles. For ceria, thirteen parameters were estimated by fitting to three experimental curves and the overall thermodynamic NO–O<sub>2</sub> equilibrium had to be respected. In addition, a qualitative criterion was for the appearance of surface species to correspond to temperature ranges known from literature. Once the parameters had been estimated, the parameter correlation matrix was evaluated, and the

**Table 3**  
Parameters for the surface reaction mechanism.

Reaction on CeO <sub>2</sub>	$A_j$ [cm,s,mol] or $S_{0,j}$	$E_j$ [kJ/mol]	Ref
<b>R1:</b>	0.75	0.00	[36]
<b>R2:</b>	$5.00 \times 10^{12}$	100	[36,32]
<b>R3:</b>	$1.00 \times 10^{-4}$	0	ts <sup>a</sup>
<b>R4:</b>	$2.00 \times 10^{12}$	175	ts
<b>R5:</b>	$5.00 \times 10^{16}$	$158-190 \theta_{\text{Ce}-\text{NO}_2} + 80 \theta_{\text{Ce}^{4+}-\text{O}}$	ts
<b>R6:</b>	$1.00 \times 10^{-8}$	0	ts
<b>R7:</b>	$1.00 \times 10^{14}$	87	ts
<b>R8:</b>	$1.00 \times 10^{15}$	50	ts
Reaction on Pt			
<b>R9:</b>	0.03	0	[34]
<b>R10:</b>	$4.00 \times 10^{27}$	$232-35 \theta_{\text{Pt}-\text{O}}$	ts
<b>R11:</b>	0.85	0	[34]
<b>R12:</b>	$5.00 \times 10^{15}$	130	ts
<b>R13:</b>	$1.00 \times 10^{21}$	115	ts
<b>R14:</b>	$7.00 \times 10^{17}$	70	ts
<b>R15:</b>	0.97	0	[34]
<b>R16:</b>	$7.00 \times 10^{11}$	88	ts

<sup>a</sup> This study.

majority of correlation coefficients are smaller than 0.7. Notably,  $A$  and  $E_a$  for a given reaction are not highly correlated, whereas all the  $\alpha_\theta$  (dependence of  $E_a$  on coverage) are more than 70% correlated with other parameters.  $A_7-E_7$  and  $A_8-E_8$  correlation coefficients are however significant, which comes as no surprise because these are surface reactions, with no measured concentration directly used in fitting.

#### 3.1. Kinetics of NO oxidation and storage over CeO<sub>2</sub>

In this section, the values obtained during calibration of the mechanism R1–R8 for the catalytic behaviour of CeO<sub>2</sub> are presented and discussed with reference to the current literature. When treated in a reducing atmosphere at high temperatures, CeO<sub>2</sub> is known to form a continuum of oxygen deficient, non-stoichiometric CeO<sub>2-x</sub> oxides ( $0 < x \leq 0.5$ ) [29]. The couple Ce<sup>4+</sup>–Ce<sup>3+</sup> exhibits redox behaviour [8], but at room temperature and high partial pressures of oxygen ( $> 10^{-5}$  bar) the affinity of Ce<sup>3+</sup> for oxygen is considerable [32]. Oxygen vacancies are thus filled by oxygen from the gas-phase [8,35] and ceria is quasi exclusively present as fully oxidised CeO<sub>2</sub>. This ready oxidation behaviour has been represented through reactions R1 and R2 by calibrating  $A_2$ . It is here seen as the only interaction of ceria with O<sub>2</sub> and therefore encloses the effects of adsorbed surface species such as peroxides and superoxides [8].  $S_{0,1}$  and  $E_2$  were kept constant at the values given in [36] and  $E_2$  was compatible with the enthalpy values given in [37,38] (see Section 3.2). The resulting value of  $A_2$  was used for all operating conditions, extrapolating its validity to partial pressures of O<sub>2</sub> higher than  $10^{-3}$  bar. Note that atomic O/Ce ratios were

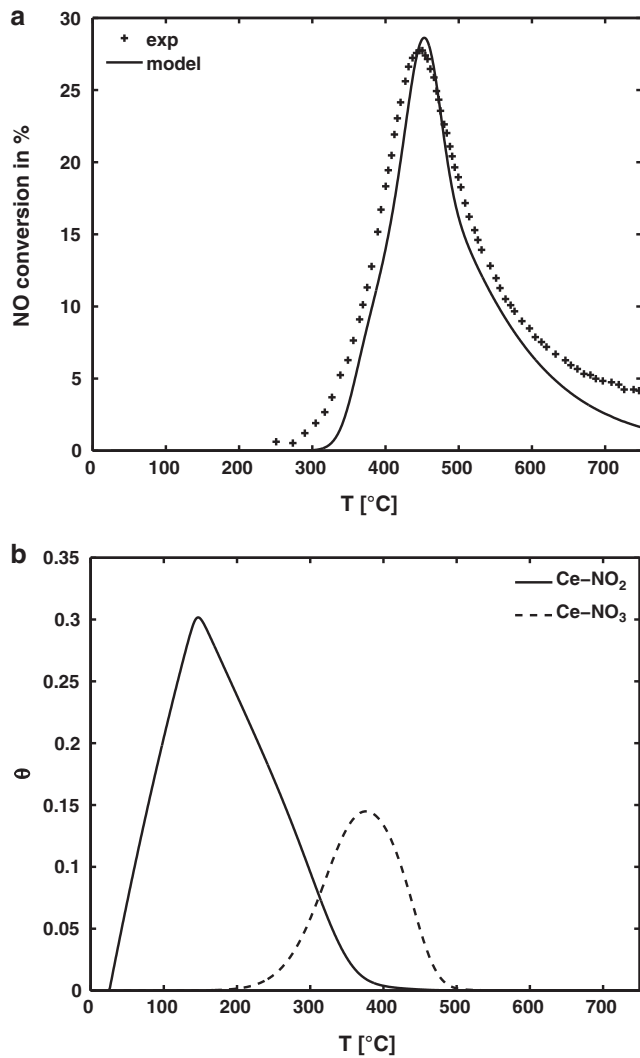


Fig. 1. Predictions of  $\text{NO}_x$  content,  $\text{NRMSD} = 8.80\%$  (a) and surface intermediates (b) during TPO of  $\text{CeO}_2$  in presence of NO and  $\text{O}_2$ . Experimental data from [33].

within 3% of the experimental values [32] at 1200 and 1725 °C at pressures of  $10^{-3}$  and  $10^{-5}$  bar.

Atribak et al. [33] published results from a 10 °C/min temperature-programmed oxidation (TPO) experiment of ceria in presence of 500 ppmv NO + 5% O<sub>2</sub> and a gas flow rate of 500 N cm<sup>3</sup>/min. The same publication also contains data from a temperature-programmed desorption (TPD) experiment under an inert gas at 10 °C/min, starting from 350 °C. The TPDs were preceded by an adsorption phase under 200 ppm NO + 5% O<sub>2</sub> at 350 °C. Both experiments were simulated using the surface area of 64 m<sup>2</sup> measured by Atribak et al. Maintaining the parameters already derived for R1 and R2, rate parameters for R3–R8 were calibrated by simulating these two experiments. Simulation results are shown in Figs. 1 and 2 and the normalised root mean square deviation (NRMSD) for the fit is 8.80%. It is known that surface nitrites result from the interaction of NO and NO<sub>2</sub> with ceria [29,33], as described by R3 and R5. These reactions are in agreement with DFT studies [17,18]. In accordance with the finding from DRIFTS data that the main pathway leading to surface nitrates is the surface oxidation of nitrites [33], the couple R7–R8 was proposed. Nitrites are readily converted into nitrates [33], resulting in the low value of  $E_7$ . Since ceria has been shown to adsorb little NO at room temperature [8], the very low value employed for the sticking coefficient  $S_{0,6}$  seems reasonable. The dependence of NO oxidation on surface

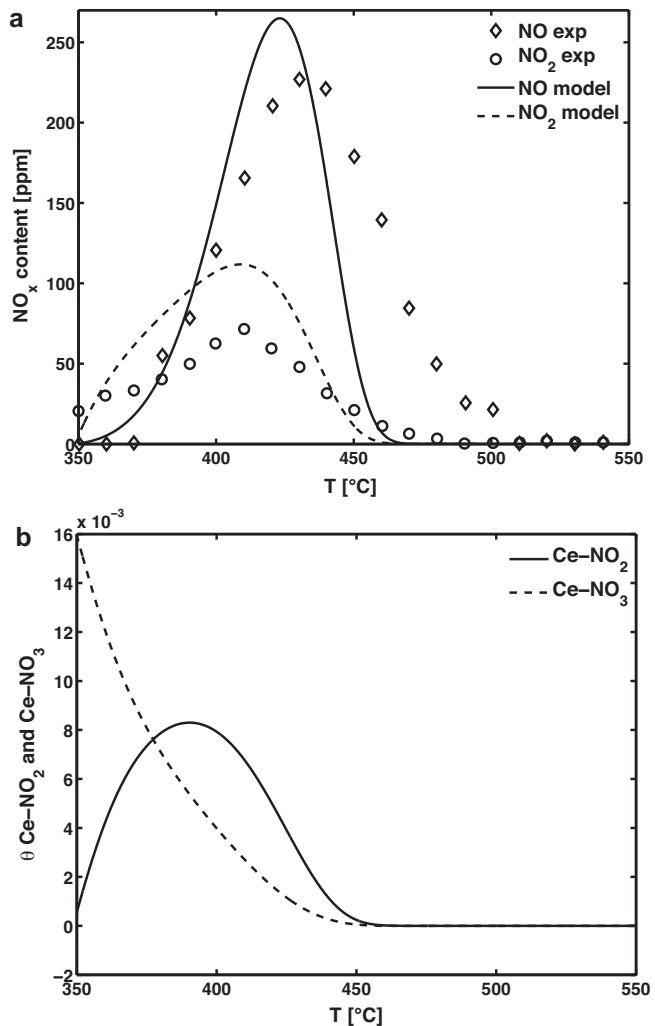
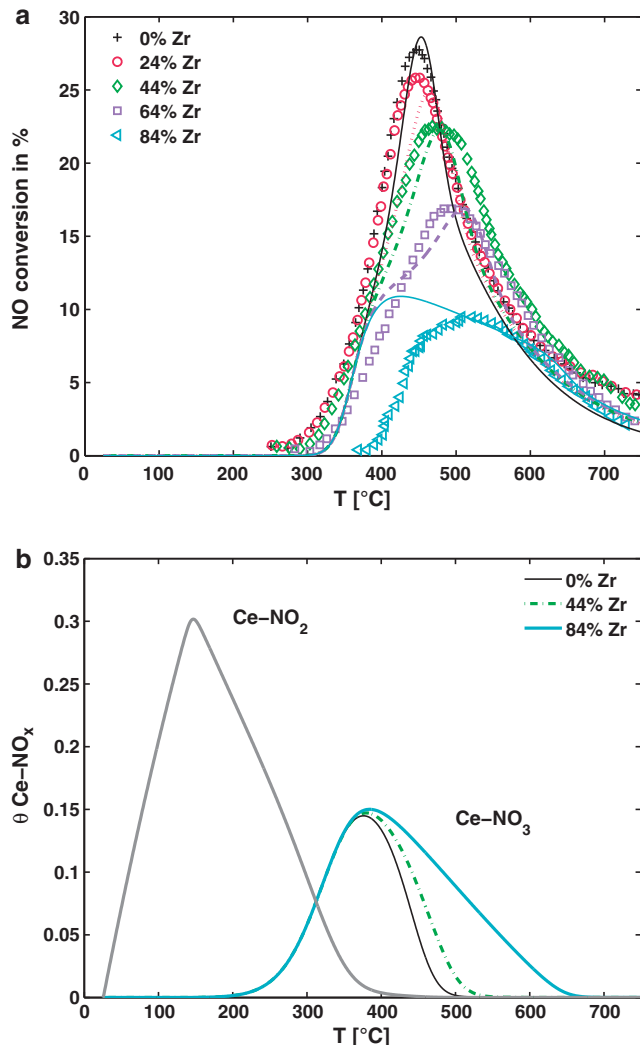


Fig. 2. Predictions of  $\text{NO}_x$  content,  $\text{NRMSD}_{\text{NO}} = 23.44\%$ ,  $\text{NRMSD}_{\text{NO}_2} = 32.62\%$  (a) and surface intermediates (b) during TPD of  $\text{CeO}_2$  under an inert flow of gas. Experimental data from [33].

coverage by various ad- $\text{NO}_x$  species [33] is here represented by the  $\theta$ -dependent value of  $E_5$ .

Given the larger rate constant of nitrite production ( $k_3 > k_7$ ) at  $T < 200$  °C, nitrites are initially formed, and transformed into nitrates starting from 200 °C (Fig. 1(b)). This is consistent with the fact, pointed out by Atribak et al., that nitrates are in general more stable than nitrites. The transformation is however reversed later on, as nitrates are changed back into nitrites to subsequently form NO and NO<sub>2</sub>. As can be seen later on (in Section 3.2, Fig. 4), the typical twin-peaked NO profile of ceria [15] can be produced with the proposed model; this is also further discussed in Section 3.4 (Fig. 9b).

Like during TPO, a nitrite peak is also formed during desorption at 350 °C (Fig. 2(b)). The tendencies of NO and NO<sub>2</sub> desorption are fairly well reproduced in Fig. 2(a). Measured curves indicate an immediate production of NO<sub>2</sub> upon exposure, whereas NO formation becomes significant only a little later, at around 370 °C. This trend is reproduced by the mechanistic parameters in Table 3. An analysis of the simulated rates of production shows that this characteristic of TPD is achieved by an increased activity of R2 due to the absence of O<sub>2</sub>. Simulations show significant production of O<sub>2</sub> by R2 during TPD, a behaviour which is confirmed by experimental observations [33]. Consequently, more Ce<sup>3+</sup> is formed, which in turn causes an immediate transformation of nitrates into nitrites (R8) and therefore NO<sub>2</sub> production (R4). The model overestimates



**Fig. 3.** Simulated and experimental [33] values of NO conversion (a) and simulated evolution of surface intermediates (b) during TPO of  $\text{Ce}_x\text{Zr}_{1-x}\text{O}_2$  in presence of NO and  $\text{O}_2$ .

$\text{NO}_2$  desorption somewhat between 360 and 400 °C, with the effect that NO formation is underestimated above 400 °C. DRIFTS spectra show that several ad-NO species, for e.g. hyponitrites, nitrites and bidentate nitrates, contribute to  $\text{NO}_x$  formation below 350 °C [39,40]. In our mechanism, these are all represented by  $\text{Ce-NO}_2$ , the only  $\text{NO}_x$ -forming species. The parameters were fitted to optimise  $\text{NO}_2$  formation in TPOs, but this meant compromising on the quality of the TPD fit. We presume that another intermediate species, reactive below 350 °C, would allow for a better fit of TPDs. For the simulations in Fig. 2(a), ad-NO<sub>x</sub> species at the start of TPD are presumed to be those stable at 350 °C, which according to a simulation of the adsorption process correspond to  $\theta_{\text{Ce-NO}_2} = 0.0005$  and  $\theta_{\text{Ce-NO}_3} = 0.0160$ . The desorption of these species yields  $\text{NO}_2$  first and then NO at higher temperatures as  $k_4 > k_5$ .

The surface nitrite,  $\text{Ce-NO}_2$ , is clearly an important intermediate species. It is involved directly in all reactions other than R1 and R2. The two products, NO and  $\text{NO}_2$ , are only produced directly from  $\text{Ce-NO}_2$ . There is thus a competition between R4, R5 and R7, who in parallel convert  $\text{Ce-NO}_2$  into  $\text{NO}_2$ , NO and  $\text{Ce-NO}_3$ , respectively. An analysis of the normalised rates of  $\text{Ce-NO}_2$  production/consumption was performed in Atribak's TPO conditions under 500 ppm NO + 5%  $\text{O}_2$ ; the results are shown in Fig. 5(a). This allows us to explain how the mechanism is able to reproduce

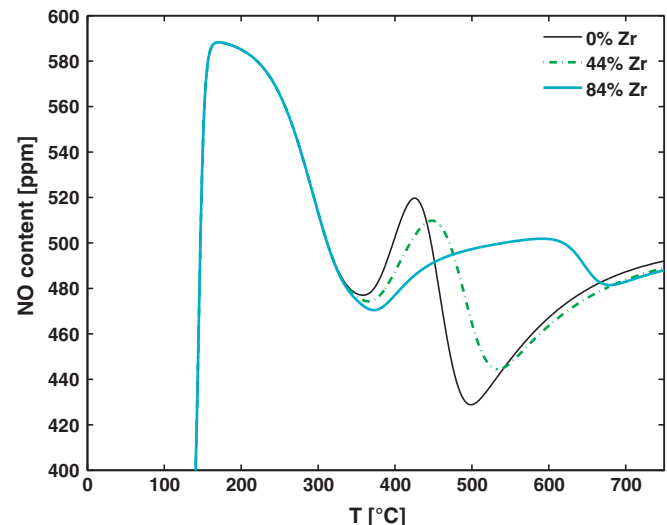


**Fig. 4.** Predictions of NO content during TPO of  $\text{Ce}_x\text{Zr}_{1-x}\text{O}_2$  in presence of NO and  $\text{O}_2$ . Feed: 500 ppmv NO + 5 %  $\text{O}_2$ .

certain particularities of  $\text{CeO}_2$ . Up to 110 °C, it is loaded with both nitrites and nitrates via R7 and R6. At 200 °C, a second nitrate storage phase (R7) begins, until R8 becomes more important due to a higher temperature (300 °C). Nitrates are then transformed back into nitrites. Above 300 °C then, the nitrites are left with only two parallel paths (R4 and R5). The importance of R4 reaches a peak at around 500 °C; up to this temperature R4 produces  $\text{NO}_2$ , but here thermodynamics takes over and R5 becomes dominant once again, in equilibrium with its reverse reaction R6. During the course of the experiment, R7 (nitrate formation) and then R4 (formation of  $\text{NO}_2$ ) momentarily outcompete R5, this results in the two peaks of NO production often observed experimentally (see also Fig. 4). In Fig. 5(b), the analysis was extended to a hypothetical case with the same conditions as in Fig. 5(a), but using 500 ppm of  $\text{NO}_2$  as reactive gas instead. In this case there is a single extended phase of nitrate storage (R7) until 300 °C and no formation of NO via R5 below 300 °C. As under  $\text{NO} + \text{O}_2$ ,  $\text{Ce-NO}_2$  is successively transformed, first into nitrates (R7) until 400 °C, then into  $\text{NO}_2$  (R4) until 450 °C and finally into NO (R5). In conclusion, the major difference between the two cases can be seen firstly at low temperatures, under 300 °C, where an analysis of R1 and R2 indicates that their net rate produces  $\text{Ce}^{4+}$  in the first case, but  $\text{Ce}^{3+}$  in the second case. The absolute value of nitrate storage rate by R7 ( $r_7$ ) then is significantly smaller than in the first case. Secondly, the shape of the rate of R7 is different in the two cases, and in particular the monotonically increasing rate in Fig. 5(b) prevents the formation of a second peak of NO. Overall, the model predicts better  $\text{NO}_x$  storage on ceria under  $\text{NO} + \text{O}_2$ , which is confirmed later on (Section 3.4). Furthermore, in this kinetic model the typical double-peak profile of NO over ceria results from a competition between R4, R5 and R7, all of which are fuelled by nitrites.

### 3.2. Kinetics of NO oxidation and storage over $\text{Ce}_x\text{Zr}_{1-x}\text{O}_2$

In this section, the results of a generalisation of the mechanism R1–R8, in order to employ it for the simulation of a series of ceria–zirconia mixed oxides, are presented. In accordance with the fact that the redox behaviour of  $\text{Ce}_x\text{Zr}_{1-x}\text{O}_2$  is dependent on Zr content, the kinetic parameters  $A_2$  and  $E_2$  were adjusted to reproduce differing behaviours in  $\text{Ce}_x\text{Zr}_{1-x}\text{O}_2$  (Fig. 3). Whereas oxidation enthalpy does not seem to vary much amongst different ceria–zirconia oxides (on average  $-\Delta H = 500 \text{ kJ/mol O}_2$  for  $0.14 < x < 0.81$ ), reduction of pure  $\text{CeO}_2$  is comparatively difficult

**Table 4**  
Kinetic parameters for  $\text{Ce}_x\text{Zr}_{1-x}\text{O}_2$ .

% Zr	$x$	$A_2$ [cm,s,mol]	$E_2$ [kJ/mol]
0	1.00	$5.00 \times 10^{12}$	100
24	0.76	$4.00 \times 10^9$	62.5
44	0.56	$2.00 \times 10^9$	62.5
64	0.36	$5.00 \times 10^8$	62.5
84	0.16	$2.00 \times 10^7$	62.5

with approximately  $-\Delta H = 800 \text{ kJ/mol O}_2$  [37,38]. Since these values apply to the fluorite-structured crystalline oxides, they are divided by eight to obtain activation energies for the single site represented in reaction R2:  $E_2 = 100 \text{ kJ/mol O}_2$  for pure  $\text{CeO}_2$ , as already proposed by Hartmann [36] and  $E_2 = 62.5 \text{ kJ/mol O}_2$  for mixed oxides. In agreement with average oxidation entropies of the mixed oxides taken from Zhou et al. [37], the proposed values of  $A_2$  decrease exponentially with Zr content. These values are summarised in Table 4.

Since the present mechanism was shown to perform well over a wide range of operating conditions, we saw it fit to perform a parametric study of Zr content. Like pure ceria, mixed oxides are expected to adsorb NO and form  $\text{Ce}-\text{NO}_2$  to then oxidise it to  $\text{Ce}-\text{NO}_3$  with increasing temperature [41]. As already mentioned in Section 2, this study focuses on kinetics, while structural aspects are described in a global manner, by an active surface. All  $\text{Ce}_x\text{Zr}_{1-x}\text{O}_2$  were presumed to have the same surface area and site density, a choice made on the consideration that BET surface area played a minor role in the NO oxidation experiments [33]. With progressively higher Zr content,  $A_2$  decreases and R3 becomes less efficient, ultimately leading to the loss in catalytic activity experimentally observed by Atribak et al. NO conversion peaks are adequately reproduced in Fig. 3(a) with NRMSDs of 8.80%, 10.09%, 11.16% and 8.25% for 0%, 24%, 44% and 64% Zr, respectively. At higher Zr contents, low temperature behaviour is predicted less accurately (NRMSD<sub>84%Zr</sub> = 42.84%), presumably because the type of nitrate formed on the  $\text{Ce}_x\text{Zr}_{1-x}\text{O}_2$  surface is also affected by Zr-doping. Azambre et al. [39] find that nitrates are more stable on Zr-rich oxides ( $x \leq 0.5$ ). Implementation of such a less reactive nitrate (either by rendering R8 less efficient, or by actually adding another nitrate species), would allow us to shift the peak in Fig. 3(a) to 500 °C as observed experimentally for  $\text{Ce}_{0.16}\text{Zr}_{0.84}\text{O}_2$ . It can be seen in Fig. 3(b), that although a change in Zr content has practically no effect on the evolution of surface nitrites, the nitrate storage phase is prolonged.

The impact of Zr content is further investigated by an analysis of normalised rates of production of  $\text{Ce}-\text{NO}_2$ . From Fig. 5(c) it can be seen that the major difference between pure ceria (Fig. 5(a)) and a mixed oxide is the peak height/ shape of R8 and R4, which results in a higher second peak of NO production (R5); NO conversion is therefore less efficient as the experimental data in Fig. 3 shows. The cause of this change in behaviour with addition of Zr is in fact the decrease of  $A_2$ , which leads to a diminished presence of  $\text{Ce}^{3+}$ ; this in turn affects R3 and R8. The latter's production of  $\text{Ce}-\text{NO}_2$  consequently slows down as observed in Fig. 5(c). As a result,  $\text{Ce}-\text{NO}_3$  is also consumed more slowly by R8, which explains the longer storage phase observed in Fig. 3(b). Atribak et al. also performed TPD for  $\text{Ce}_{0.24}\text{Zr}_{0.76}\text{O}_2$ . The directions of the changes are reproduced by the model (Fig. 6), although the predicted extent of change is somewhat smaller. As for the TPD of pure  $\text{CeO}_2$  (Fig. 2, shown again for comparison in Fig. 6), NO is overpredicted for 24% Zr (NRMSD = 33.78%). NO<sub>2</sub> however is underpredicted (NRMSD = 24.10%). This is even more marked for mixed oxides with more Zr, and as in the case of the NO-TPO over  $\text{Ce}_{0.16}\text{Zr}_{0.84}\text{O}_2$ , we can presume that Zr-doping affects nitrate stability and that this must necessarily be taken into account to

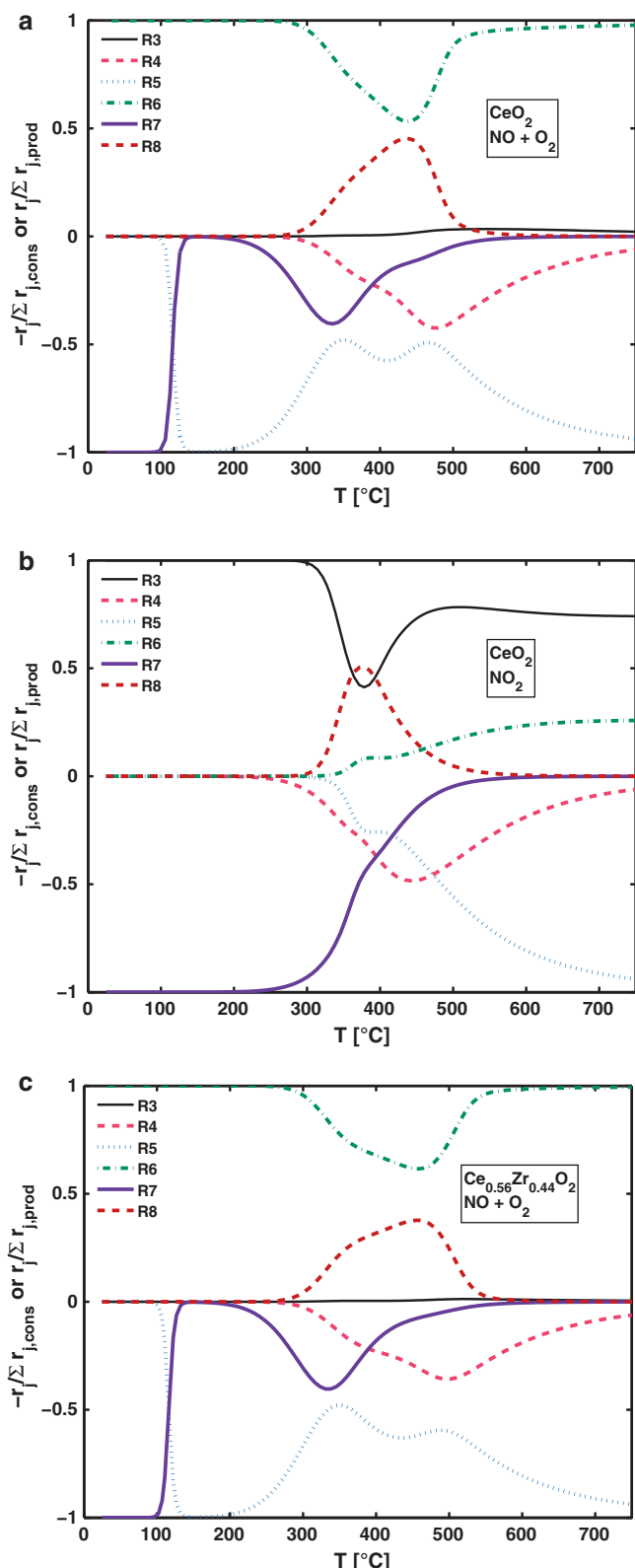


**Fig. 5.** Normalised rates of production/consumption of  $\text{Ce}-\text{NO}_2$  during simulation of the TPO of (a)  $\text{CeO}_2$  with  $\text{NO} + \text{O}_2$ , (b)  $\text{CeO}_2$  with  $\text{NO}_2$  and (c)  $\text{Ce}_{0.56}\text{Zr}_{0.44}\text{O}_2$  with  $\text{NO} + \text{O}_2$ .

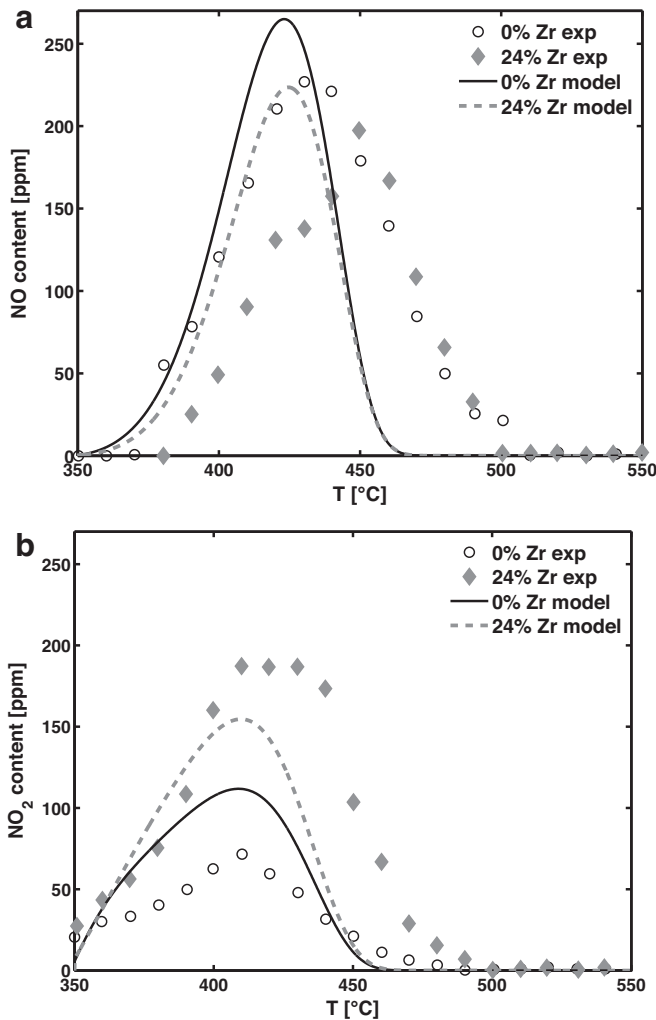


**Fig. 6.** Predictions of  $\text{NO}_x$  content during TPD of  $\text{Ce}_x\text{Zr}_{1-x}\text{O}_2$  under an inert flow of gas. 24% Zr:  $\text{NRMSD}_{\text{NO}} = 33.78\%$ ,  $\text{NRMSD}_{\text{NO}_2} = 24.10\%$ . Experimental data from [33].

correctly predict TPD behaviour for 84% Zr and above. In summary, simulations using the kinetic parameters derived during the course of this study are in agreement with catalytic experiments from disparate sources. The model is in particular capable of correctly predicting NO oxidation behaviour of various ceria–zirconia mixed oxides ( $\% \text{Zr} \leq 64\%$ ) over a range of temperatures and adsorption/TPD behaviour over  $\text{CeO}_2$ .

### 3.3. Kinetics of NO oxidation over $\text{Pt}/\text{Al}_2\text{O}_3$

We provided details on the mechanism R9–R16 in a previous publication [11]. The updated parameters are shown in Table 3. The interaction of Pt with  $\text{O}_2$  (R9–R10) was modelled on the TPD performed by Olsson et al. [34] and the resulting fit shown in Fig. 7.  $\text{O}_2$  evolution in the gaseous phase is adequately reproduced, as is the profile of surface oxygen modelled by the authors of the original article. R11–R16 were calibrated using the experimental NO and  $\text{NO}_2$  values in Fig. 8. Overall, the fit is reasonable, although the low-temperature reactivity is underestimated. Other studies also indicate that reactions R9–R16 allow for prediction of the overall trend, but are not sufficient to reproduce activity below  $200^\circ\text{C}$  [42,34]. Note that the  $\text{Pt}/\text{Al}_2\text{O}_3$  surface displays a peak of Pt–NO between 150 and  $250^\circ\text{C}$ , but  $\text{NO}_x$  storage on Pt remains negligible ( $\theta_{\text{Pt–NO}_2} < 0.05$  between 0 and  $500^\circ\text{C}$ ) in comparison to ceria–zirconia.

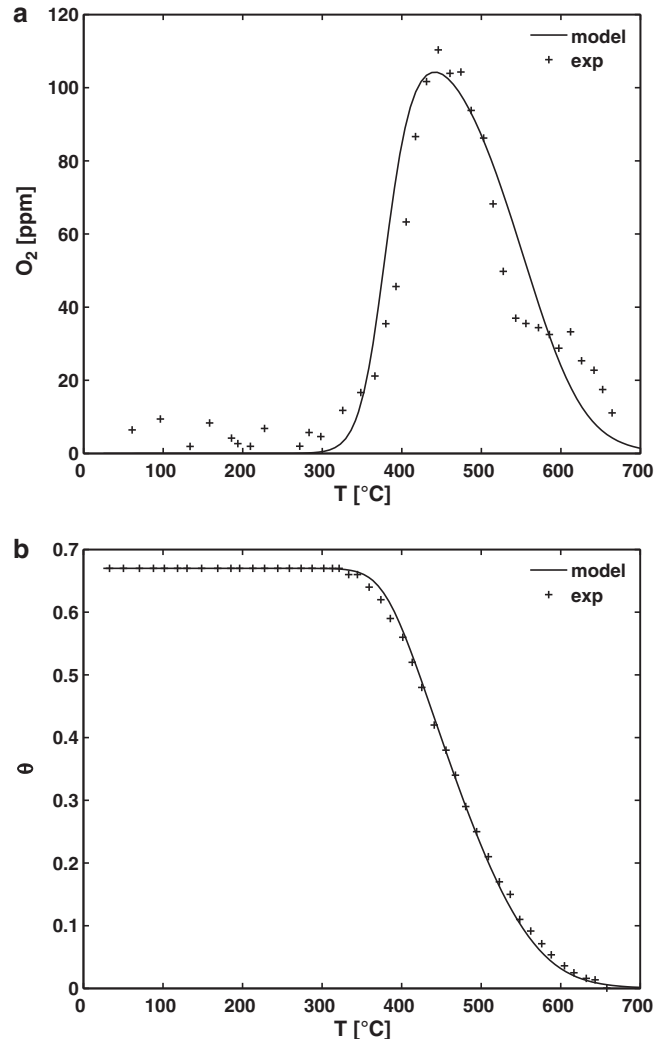


**Fig. 7.** Predictions of  $\text{O}_2$  content,  $\text{NRMSD} = 10.88\%$  (a) and surface intermediates (b) during TPD of platinum,  $\text{NRMSD} = 1.20\%$ . Experimental data from [34].

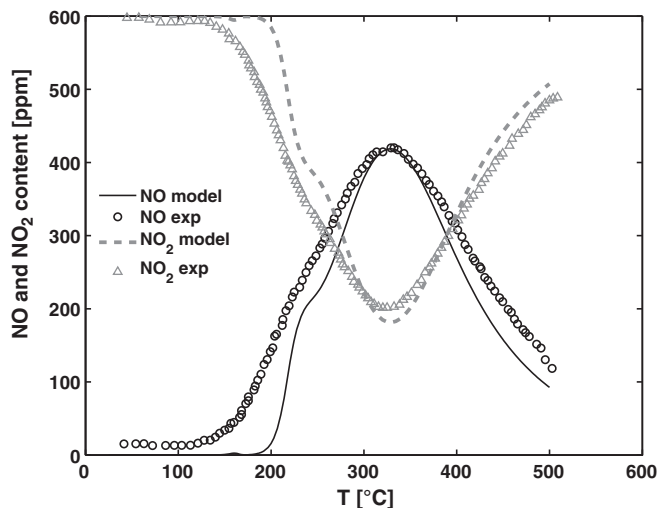


**Fig. 8.** Predictions of  $\text{NO}_x$  evolution during TPO of platinum in presence of NO and  $\text{O}_2$ ,  $\text{NRMSD}_{\text{NO}} = 13.11\%$ ,  $\text{NRMSD}_{\text{NO}_2} = 13.71\%$ . Experimental data from [34].

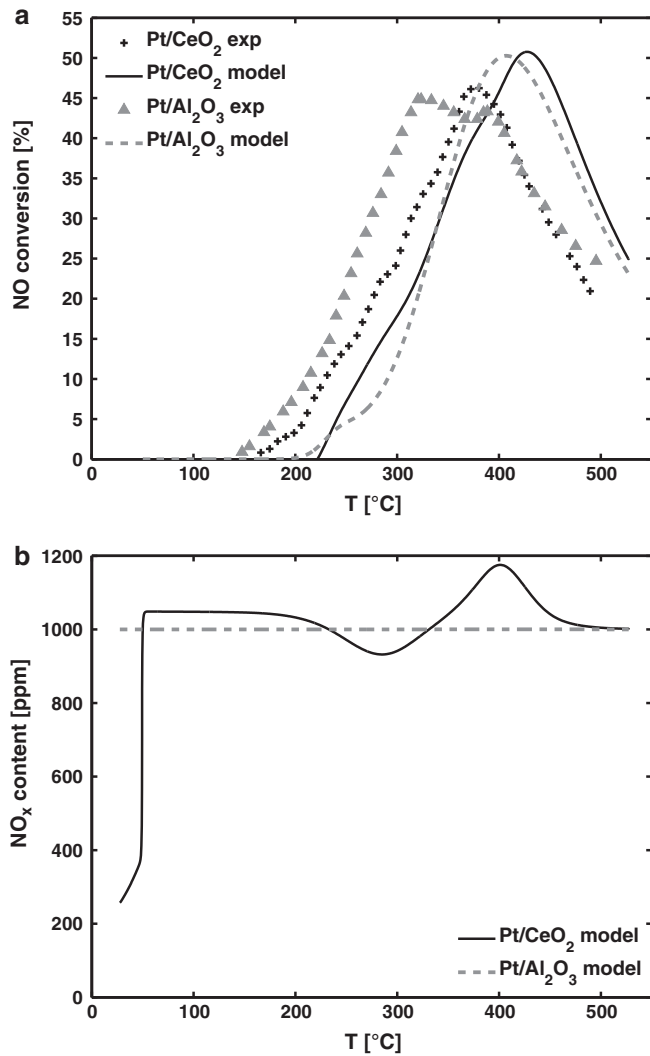


**Fig. 9.** Predicted and experimental curves for the oxidation of 1000 ppmv NO in 20% O<sub>2</sub> over Pt/CeO<sub>2</sub> (NRMSE = 20.94%) and Pt/Al<sub>2</sub>O<sub>3</sub> (NRMSE = 34.40%). Experimental data from [21].

#### 3.4. NO oxidation and storage over Pt/CeO<sub>2</sub>

The feasibility of coupling reaction mechanisms for CeO<sub>2</sub> (R1–R8) and Pt/Al<sub>2</sub>O<sub>3</sub> (R9–R16) in order to simulate Pt/CeO<sub>2</sub> or Pt/CeO<sub>2</sub>/Al<sub>2</sub>O<sub>3</sub> was studied. To our knowledge, the only study which reports on the catalytic activity of Pt/CeO<sub>2</sub> for oxidation of NO in a gas flow containing NO and O<sub>2</sub> alone, is an article by Benard et al. [21]. The authors of the study carried out experiments in the same conditions for both Pt/CeO<sub>2</sub> (Cat1) and Pt/Al<sub>2</sub>O<sub>3</sub> (Cat2). Both experiments were simulated and are shown in Fig. 9(a). The surface areas of CeO<sub>2</sub> and Pt resulting from the calculation are 3.5 m<sup>2</sup> and 1.72 × 10<sup>-4</sup> m<sup>2</sup> (Cat1 and Cat2), respectively. The latter corresponds to a dispersion of 0.03% calculated using the area of one Pt site (8.00 × 10<sup>-20</sup> m<sup>2</sup>/atom from [34]) and a weight fraction of 1% Pt as measured by Benard et al. Since a typical Pt dispersion on ceria is about 20% [43,21], it must be presumed that all of the surface area of the 200 mg of catalyst used in the experiment was not accessible. The fits in Fig. 9(a) are reasonable, considering that the kinetic parameters used for the simulation were derived from experiments in very different operating conditions and featuring differently synthesised catalysts. Position in temperature is not altogether correctly simulated, but peak shapes and heights are fairly well reproduced, as well as the fact that the major difference

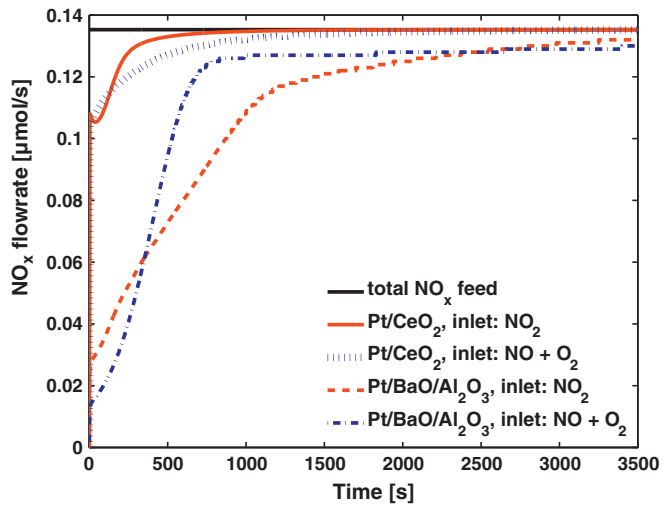


**Fig. 10.** Predicted NO<sub>x</sub> evolution over Pt/CeO<sub>2</sub> and Pt/BaO/Al<sub>2</sub>O<sub>3</sub>. Feed: 1000 ppmv NO + 3% O<sub>2</sub> (blue lines), 1000 ppmv NO<sub>2</sub> (red lines). Operating conditions from [11,45]. (For interpretation of the references to color in this figure legend, the reader is referred to the web version of the article.)

between Pt/Al<sub>2</sub>O<sub>3</sub> and Pt/CeO<sub>2</sub> in NO oxidation is a very slight temperature shift [44,21]. Note that the slight double peak for Cat2 is not always seen to be a characteristic of NO oxidation over this catalyst (e.g. [34]). Clearly, reactivity between 100 and 200°C is again underpredicted as it was for Pt/Al<sub>2</sub>O<sub>3</sub> in this and other studies. In particular, the “wavy”shape of the ascending slope for Cat1 is captured. As found in Section 3.1, this profile (also observed in Figs. 4 and 9(b)) arises because Ce-NO<sub>2</sub> is successively channelled into nitrates and NO<sub>2</sub>, leaving fewer nitrites as an input for NO production at 350 and 450°C circa. The shape of the “wavy”NO profile is attenuated by the presence of Pt. Overall, NO oxidation over Pt/CeO<sub>2</sub> differs very little from that over Pt/Al<sub>2</sub>O<sub>3</sub> and the advantage of ceria appears to be mainly its storage capacity.

Storage behaviour of Pt/CeO<sub>2</sub> was further studied by comparing it to that of Pt/BaO/Al<sub>2</sub>O<sub>3</sub>, which we have modelled previously [11,12] and investigating the impact of NO + O<sub>2</sub> versus NO<sub>2</sub> feed. A steady state (constant *T* and feed composition) experiment performed by Scotti et al. [45] was chosen as appropriate for quantifying storage behaviour. As shown in Fig. 10, when modelling NO<sub>x</sub> storage and oxidation [12], BaO stored 1.17 and 1.48 mol NO<sub>x</sub>/mol of storage sites for NO + O<sub>2</sub> and NO<sub>2</sub> feeds, respectively. In the same conditions, CeO<sub>2</sub> stored 0.22 and 0.12 mol NO<sub>x</sub>/mol, in agreement with the finding for more complex gas feeds that Ba stores more efficiently than CeO<sub>2</sub> [46–48]. It is well known that more basic supports store more NO<sub>x</sub> [49,50] and our model reproduces this trend. Pt/CeO<sub>2</sub> stores NO<sub>x</sub> better in presence of NO and O<sub>2</sub>, although the difference is small, whereas Pt/BaO stores more efficiently in presence of NO<sub>2</sub>. Note that the comparison was made using the same amount of active storage sites for both catalysts. These results also confirm the finding in Section 3.1 that NO/O<sub>2</sub> co-adsorption on ceria is more efficient. As pointed out earlier, the couple R1–R2 produces lattice oxygen (Ce<sup>4+</sup>–O) when exposed to the NO + O<sub>2</sub> feed, thereby facilitating the storage of nitrates (Ce-NO<sub>3</sub>) via R7. Under an NO<sub>2</sub> feed, the only oxygen available is that of the lattice, which is consequently consumed by R1–R2, thereby deteriorating storage by R7.

#### 4. Conclusion

A detailed kinetic surface mechanism for the oxidation and storage of NO<sub>x</sub> over platinum-, ceria- and ceria-zirconia-based catalysts was validated against experimental data from literature.

The mechanism was coupled with a fixed-bed reactor model in order to extract the kinetic parameters. It was shown to perform well for data from different sources and operating conditions. The kinetic parameters obtained allow reproduction of the main trends of  $\text{NO} + \text{O}_2$  desorption, NO oxidation and  $\text{NO}_x$  storage on the various catalysts. Storage on ceria and ceria-zirconia in the shape of nitrates stable until 350 °C is sufficient to reproduce  $\text{NO} + \text{O}_2$  TPOs for  $\% \text{Zr} \leq 64\%$  and TPDs over pure  $\text{CeO}_2$ . However, a more detailed description involving at least one more N-surface species would probably improve TPD simulation. Efficiency of NO oxidation over ceria-based catalysts decreases with Zr content (0–64 mol%) and therefore depends on redox behaviour of the oxide, as demonstrated by the different values of kinetic parameters in the mechanism for ceria-zirconia catalysts. But above 64% Zr, it becomes necessary to take into account the effect of Zr-doping on the stability of nitrates. It was shown that it is possible to estimate detailed kinetic parameters for NO oxidation over platinum and ceria separately and obtain a reasonable prediction of the behaviour of  $\text{Pt}/\text{CeO}_2$  by combining these parameters. When coupling platinum and ceria, oxidation behaviour is dictated by Pt, but storage occurs over ceria.  $\text{BaO}$  remains a more efficient storage component than  $\text{CeO}_2$ , when considering an equal number of active sites, and unlike  $\text{BaO}$ , ceria stores NO (in presence of  $\text{O}_2$ ) more efficiently than  $\text{NO}_2$ .

## Acknowledgements

K.L. is grateful to IFP Energies nouvelles and ANRT (CIFRE programme) for the financial support received.

## References

- [1] S. Roy, A. Baiker, *Chem. Rev.* 109 (2009) 4054–4091.
- [2] B.A. van Setten, M. Makkee, J. Moulijn, *Catal. Rev. Sci. Eng.* 43/44 (43) (2001) 489–564.
- [3] L. Retailleau, R. Vonarb, V. Perrichon, E. Jean, D. Bianchi, *Energy Fuels* 18 (2004) 872–882.
- [4] A. Trovarelli, C. de Leitenburg, M. Boaro, G. Dolcetti, *Catal. Today* 50 (1999) 353–367.
- [5] S. Miyoshi, H. Yamada, H. Iwakuni, K. Harada, K. Minoschima, A. Takami, *Exhaust Gas Purification Catalyst and Method of Fabricating the Same*, US Patent No. 2007/0117715 A1 (2007).
- [6] G. Blanchard, E. Rohart, Y. Lendresse, F. Tronel, X. Courtois, D. Duprez, S. Elbouazzaoui, P. Marecot, *Zirconium/Praseodymium Oxide  $\text{NO}_x$  Traps and Purification of Gases Containing Nitrogen Oxides ( $\text{NO}_x$ ) Therewith*, US Patent No. 2009/0191108 A1 (2009).
- [7] L.J. Gill, P.G. Blakeman, M.V. Twigg, A.P. Walker, *Top. Catal.* 28 (2004) 157–164.
- [8] A. Trovarelli (Ed.), *Catalysis by Ceria and Related Materials*, Imperial College Press, 2002.
- [9] G.B. Fisher, J.R. Theis, M.V. Casarella, S.T. Mahan, *SAE Trans.* 102 (1993).
- [10] J.R. Theis, W.J. LaBarge, G.B. Fisher, *SAE Trans.* 102 (1993).
- [11] N. Rankovic, A. Nicolle, P. Da Costa, *J. Phys. Chem. C* 114 (2010) 7102–7111.
- [12] N. Rankovic, A. Nicolle, D. Berthout, P. Da Costa, *Catal. Commun.* 12 (2010) 54–57.
- [13] Y. Ji, T. Toops, U. Graham, G. Jacobs, M. Crocker, *Catal. Lett.* 110 (2006) 29–37.
- [14] E. Rohart, V. Bellière-Baca, K. Yokota, V. Harlé, C. Pitois, *Top. Catal.* 42/43 (2007) 71–75.
- [15] R. Marques, P. Darcy, P. Da Costa, H. Mellottée, J.-M. Trichard, G. Djéga-Mariadassou, *J. Mol. Catal. A: Chem.* 221 (2004) 127–136.
- [16] M. Nolan, S.C. Parker, G.W. Watson, *Phys. Chem. Chem. Phys.* 8 (2006) 216–218.
- [17] M. Nolan, S.C. Parker, G.W. Watson, *J. Phys. Chem. B* 110 (2006) 2256–2262.
- [18] Z. Yang, T.K. Woo, K. Hermansson, *Surf. Sci.* 600 (2006) 4953–4960.
- [19] V. Schmeißer, J. de Riva Pérez, U. Tuttles, G. Eigenberger, *Top. Catal.* 42/43 (2007) 15–19.
- [20] Y. Ji, J.-S. Choi, T. Toops, M. Crocker, M. Naseri, *Catal. Today* 136 (2008) 146–155.
- [21] S. Benard, L. Retailleau, F. Gaillard, P. Vernoux, A. Giroir-Fendler, *Appl. Catal., B* 55 (2005) 11–21.
- [22] R.J. Berger, F. Kapteijn, J.A. Moulijn, G.B. Marin, J. De Wilde, M. Olea, D. Chen, A. Holmen, L. Lietti, E. Tronconi, Y. Schuurman, *Appl. Catal. A* 342 (2008) 3–28.
- [23] R.J. Gorte, *J. Catal.* 75 (1982) 164–174.
- [24] P. Wellstead, *Introduction to Physical System Modelling*, Academic Press Ltd., 1979.
- [25] H. Wang, B. Drugogorski, E.M. Kennedy, *Prog. Energy Combust. Sci.* 29 (2003) 487–513.
- [26] K. Leistner, A. Nicolle, D. Berthout, P. da Costa, *Combust. Flame* (2011), doi:10.1016/j.combustflame.2011.06.006.
- [27] O. Deutschmann, *Interactions between transport and chemistry in catalytic reactors*, Habilitation thesis, 2001.
- [28] M. Coltrin, R. Kee, F. Rupley, *Surface Chemkin (Version 4.0): A Fortran Package for Analyzing Heterogeneous Chemical Kinetics at a Solid-Surface–Gas-Phase Interface*, Report SAND90-8003B, Sandia National Laboratories, 1990.
- [29] A. Trovarelli, *Catal. Rev. Sci. Eng.* 38 (1996) 439–520.
- [30] M. Daturi, E. Finocchio, C. Binet, J.-C. Lavalle, F. Fally, V. Perrichon, H. Vidal, N. Hickey, J. Kašpar, *J. Phys. Chem. B* 104 (2000) 9186–9194.
- [31] L. Olsson, B. Andersson, *Top. Catal.* 28 (2004) 89–98.
- [32] M. Zinkevich, D. Djurovic, F. Aldinger, *Solid State Ionics* 177 (2006) 989–1001.
- [33] I. Atribak, B. Azambre, A. Bueno-López, A. García-García, *Appl. Catal. B* 92 (2009) 126–137.
- [34] L. Olsson, H. Persson, E. Fridell, M. Skoglundh, B. Andersson, *J. Phys. Chem. B* 105 (2001) 6895–6906.
- [35] I. Atribak, B. Azambre, A. Bueno-López, A. García-García, L. Zenbury, P. Burg, in: *Catalysis for Environment—International Group for Research (GDRI) Meeting*.
- [36] M. Hartmann, *Untersuchung der Ceroxid-Speicherkomponente von  $\text{NO}_x$ -Speicherkatalysatoren*, Master's thesis, Universität Karlsruhe, 2006.
- [37] G. Zhou, P.R. Shah, T. Kim, P. Fornasiero, R.J. Gorte, *Catal. Today* 123 (2007) 86–93, M. Albert Vannice Festschrift.
- [38] G. Zhou, P.R. Shah, T. Montini, P. Fornasiero, R.J. Gorte, *Surf. Sci.* 601 (2007) 2512–2519.
- [39] B. Azambre, L. Zenbourg, A. Koch, J. Weber, *J. Phys. Chem. C* 113 (2009) 13287–13299.
- [40] B. Azambre, L. Zenbourg, F. Delacroix, J. Weber, *Catal. Today* 137 (2008) 278–282.
- [41] M. Adamowska, A. Krzton, M. Najbar, P.D. Costa, G. Djéga-Mariadassou, *Catal. Today* 137 (2008) 288–291, AWPA Symposium 2007.
- [42] D. Bhatia, R.W. McCabe, M.P. Harold, V. Balakotaiah, *J. Catal.* 266 (2009) 106–119.
- [43] V. Perrichon, L. Retailleau, P. Bazin, M. Daturi, J.C. Lavalle, *Appl. Catal. A* 260 (2004) 1–8.
- [44] G. Zafiris, R. Gorte, *Surf. Sci.* 276 (1992) 86–94.
- [45] A. Scotti, I. Nova, E. Tronconi, L. Castoldi, L. Lietti, P. Forzatti, *Ind. Eng. Chem. Res.* 43 (2004) 4522–4534.
- [46] E. Corbos, S. Elbouazzaoui, X. Courtois, N. Bion, P. Marecot, D. Duprez, *Top. Catal.* 42/43 (2007) 9–13.
- [47] Y. Ji, T. Toops, M. Crocker, *Catal. Lett.* 119 (2007) 257–264.
- [48] P. Svedberg, E. Jobson, S. Erkfeldt, B. Andersson, M. Larsson, M. Skoglundh, *Top. Catal.* 30/31 (2004) 199–206.
- [49] D. Martin, D. Duprez, *J. Mol. Catal. A: Chem.* 118 (1997) 113–128.
- [50] M. Piacentini, M. Maciejewski, A. Baiker, *Top. Catal.* 42/43 (2007) 55–59.